Regularity diagnostics
applied to a turbulent boundary layer

By H. J. Bae, J. D. Gibbon†, R. M. Kerr‡ AND A. Lozano-Durán

Regularity diagnostics for the Navier-Stokes equations based on rescaled high-order vorticity moments are applied to direct numerical simulation (DNS) of plane turbulent channel flow and calculations of high-Reynolds-number vortex reconnection. At the wall-normal height typical of the tips of hairpin vortices, the temporal evolution of the vorticity moments is qualitatively similar to that of controlled high-Reynolds-number vortex reconnection in the absence of walls. Both the channel flow and vortex reconnection data exhibit higher measure of vorticity than previous results from decaying and forced isotropic turbulence. This allows for future analysis of vortex dynamics based on new results detailing the vorticity and helicity dynamics of reconnection events.

1. Introduction

In analysis of numerical turbulence, the maximum vorticity, $\omega_p = \|\omega\|_\infty$, and enstrophy, $Z = \|\omega\|_2^2/V$, have historically been the main quantities of interest, where ω is vorticity and V is the volume of the computational domain. Although enstrophy is physically meaningful given its proportionality to the energy dissipation rate, for many years, the best bound for singular growth was provided by ω_p, with the caveat that the bound has a large prefactor that is dependent on the size of the periodic computational box (Kerr 2018b). By extending the analysis to the strain and production terms of the Cayley-Hamilton framework (Ashurst *et al.* 1987), a more complete description in terms of the reduced Vieillefosse/restricted Euler equations can be made. However, this reduced model neglects pressure effects. Indeed, it has been observed numerically that the Euler equations do not display singular behaviors (see Kerr 2013a, and references therein).

An approach that avoids the direct accounting of pressure is to use the rescaled vorticity moment hierarchy given by

$$\Omega_m(t) = \left(V^{-1} \int_{\mathcal{V}} |\omega|^{2m} \mathrm{d}V \right)^{1/(2m)} , \tag{1.1}$$

for which (kinematically) $\Omega_{m+1} \geq \Omega_m$ always holds due to Hölder's inequality.

To address the dynamics of the Navier-Stokes equations using time inequalities, a more convenient rescaling is given by

$$D_m(t) = \left[\varpi_0^{-1} \Omega_m(t) + 1 \right]^{\alpha_m} , \quad \alpha_m = \frac{2m}{4m - 3} , \tag{1.2}$$

where ϖ_0 is a relevant frequency as defined by Gibbon *et al.* (2014). From a variety of numeric experiments with periodic boundary conditions, it has been observed that the D_m are almost always ordered on a descending scale such that $D_{m+1} < D_m$ for $m \geq 1$.

† Department of Mathematics, Imperial College, UK
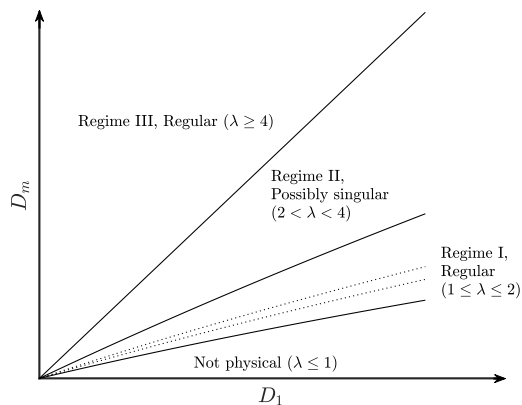‡ School of Engineering, Warwick University, UK

FIGURE 1. The regimes in the D_1–D_m plane. Regime I is bound by the lower concave curve ($\lambda = 1$) derived from Hölder's inequality and the upper concave curve ($\lambda = 2$), which is the upper limit of the regular regime. The dotted curves approximately denote the region where previous computations lie.

This property derives from the fact that D_m can be parametrically written in terms of D_1 such that

$$D_m = D_1^{A_{m,\lambda}}, \quad A_{m,\lambda} = \frac{[\lambda_m(t) - 1](m-1) + m}{4m - 3}, \tag{1.3}$$

where $1 \leq \lambda_m \leq 4$ is a set of time-dependent parameters (Gibbon *et al.* 2014). Eq. (1.3) can be interpreted in the following manner: instead of considering the magnitude of members of the sequence $\{D_1, D_2, D_3, \ldots, D_m\}$ as functions of time, the magnitude of D_m with respect to D_1 is measured using the parameters $\lambda_m(t)$. Thus, we have the sequence $\{D_1, \lambda_2, \lambda_3, \ldots, \lambda_m\}$, which is parameterized by the relative logarithmic ratio

$$\lambda_m = \frac{(4m - 3) \log D_m / \log D_1 - 1}{m - 1}, \tag{1.4}$$

as illustrated in Figure 1. Regime I ($1 \leq \lambda_m \leq 2$) is regular, whereas solutions in Regime II ($2 \leq \lambda_m \leq 4$) are potentially singular. In Gibbon *et al.* (2014), $\lambda_m \leq 1.2$ is observed for almost all of the times in periodic forced and decaying turbulent flows. Exceptions were found for decaying turbulence when enstrophy had its maximum growth with $\lambda_m \approx 1.25$ and a low Reynolds number version of the reconnection calculation here when there was a brief spurt with $\lambda_m \approx 1.3$.

In the present work, we identify transient events with higher λ_m, indicative of stronger enstrophy growth, and provide comparisons suggesting that the tips of the boundary layer hairpin vortices are commensurable with vortex reconnection events. The paper is organized as follows. In Section 2, in order to isolate the dynamics of mutual interaction among vortical motions, we describe the anti-parallel reconnection event and apply the regularity diagnostics. Section 3 presents the turbulent channel flow simulations and the regularity diagnostics applied to the channel flow. Section 4 introduces the invariants of the velocity gradient tensor (R and Q), and regularity diagnostics results are conditioned to the (R, Q) phase plane. Section 5 focuses on the similarities between hairpins and reconnection events, concluding that the tips of the boundary layer hairpin vortices are consistent with reconnection events. The paper concludes with a summary in Section 6.
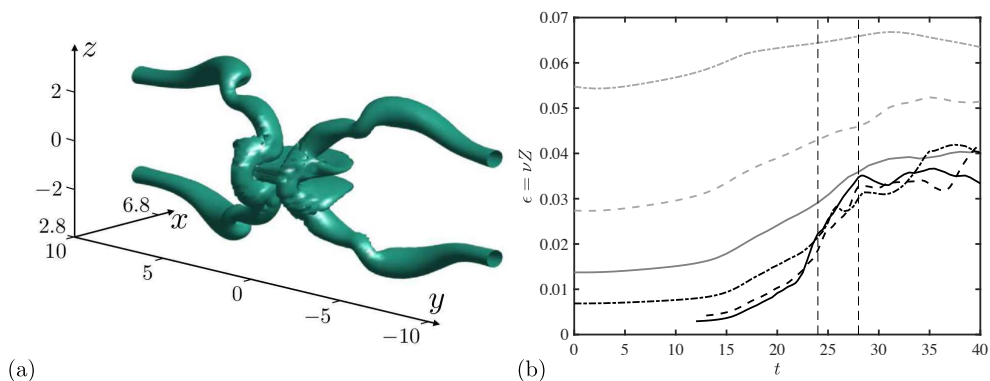
FIGURE 2. (a) Three-dimensional isosurfaces of the anti-parallel vortices at $t = 24$. (b) Growth of the dissipation $\epsilon = \nu Z$ for $\nu = 2 \times 10^{-3}$ (gray dot dashed), 1×10^{-3} (gray dashed), 5×10^{-4} (gray solid), 2.5×10^{-4} (black dot dashed), 1.25×10^{-4} (black dashed), and $\nu = 9 \times 10^{-5}$ (black solid). Times $t = 24$ and $t = 28$ are given by straight dashed lines.

2. Anti-parallel reconnection

The data obtained are from DNS of an anti-parallel vortex reconnection event with three periodic dimensions for kinematic viscosity, ν, ranging from 2×10^{-3} to 9×10^{-5} (Kerr 2018b). The initial vortices, aligned along the z axis with axial direction y, are propagated in the x direction as in Kerr (2013b), where an internal vorticity profile and a symmetric perturbation of the trajectory are designed to avoid the internal instabilities. This allows the axial direction to be expanded in a manner such that the initial dynamics near $y = 0$ are not be immediately affected. The simulation utilizes the symmetric filtered pseudo-spectral calculations, and Figure 2(a) shows the full symmetrized configuration at one time instance. The symmetric quadrants used for the calculations in Figure 2 are $(L_x, L_y, L_z) = (4\pi, 4\pi, 2\pi)$ for $\nu = 2 \times 10^{-3}$ and 1×10^{-3}, $(L_x, L_y, L_z) = (4\pi, 4\pi, 4\pi)$ for $\nu = 5 \times 10^{-4}$ to 1.25×10^{-4} and $(L_x, L_y, L_z) = (4\pi, 4\pi, 6\pi)$ for $\nu = 9 \times 10^{-5}$. The domain size is adjusted to maintain a ν-independent convergence of the $\sqrt{\nu}Z$ scaling regime at the end of the reconnection event, as first identified for trefoils in Kerr (2018a) and further discussed for the anti-parallel vortex reconnection cases in Kerr (2018b).

The reconnection in Kerr (2018b) approximately spans the period $16 \leq t \leq 24$, where the nonlinear timescale is $t_f = \delta_z^2/\Gamma \approx 3.2$ with Γ being the initial circulation of the vortices and δ_z their initial separation in z. During the reconnection, the dissipation rate $\epsilon = \nu Z(t)$ grows linearly as shown in Figure 2(b), particularly for $\nu \leq 5 \times 10^{-4}$. For $\nu \leq 1.25 \times 10^{-4}$ there is a burst in the growth of ϵ up to $t \approx 28$. At $t \approx 30$, a roughly steady ν-independent ϵ begins to appear. The dissipation rate ϵ rather than $\sqrt{\nu}Z$ is plotted in Figure 2(b) to investigate whether a finite dissipation anomaly, that is, finite $\Delta E = \int_0^T \epsilon dt$ by a fixed time T as $\nu \to 0$, is beginning to form. A collection of vortex rings propagating in x could be the structures responsible for the strong $24 \leq t \leq 28$ growth of ϵ that could be consistent with a dissipation anomaly, developing in a finite time T, without evidence for singularities of any form.

The regularity diagnostic, in particular the computation of λ_m from Eq. (1.4), is applied to the reconnection event (Figure 3a). In contrast to previous computations discussed in the introduction, the new high-Reynolds-number reconnection calculations (Kerr 2018b)
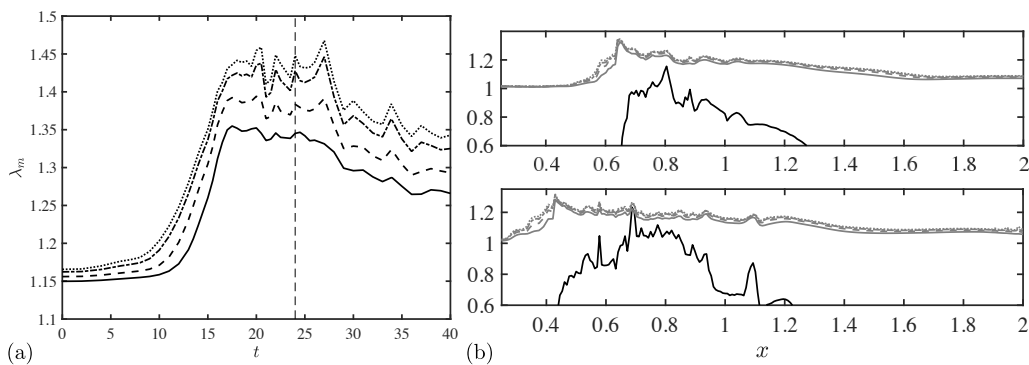
FIGURE 3. (a) Broad temporal peak of $\lambda_m(t)$ for $m = 2$ (solid), 3 (dashed), 4 (dot-dashed), 5 (dotted) during reconnection. Time $t = 24$ given by straight dashed line. (b) Comparison of λ_m, $m = 2, 3, 4, 5$ (gray lines) and $\log(\omega_p)/4$ (black solid line) as a function of x for $t = 20$ (bottom) and $t = 24$ (top).

display larger peak values of $\lambda_m > 1.45$. However, $\lambda_m < 2$ for all times, which is an indication of regularity.

The regularity diagnostic is repeated by integrating in the y, z direction only, such that

$$\Omega_m(x, t) = \left(\frac{1}{L_y L_z} \int \int |\omega|^{2m} \mathrm{d}y \mathrm{d}z \right)^{1/(2m)} \tag{2.1}$$

is a function of the propagation direction x and t. The quantities D_m and λ_m are computed analogously. Figure 3(b) illustrates the vorticity profiles in x using ω_p and λ_m. The profiles of other vorticity diagnostics, including the enstrophy and its production R_ω, are not shown here as they are similar to ω_p. Note that the leading edge location of the $\log(\omega_p)$ profile (scaled for better comparison with λ_m) coincides with the maxima of λ_m.

Figure 3 provides the specific footprint of reconnection events identified in periodic domains. In the next section, the nature of the vorticity and λ_m profiles extracted for hairpin vortices from a turbulent boundary layer is compared to those in Figure 3(b).

3. Turbulent channel flow

The data obtained are from DNS of a plane turbulent channel flow with two periodic directions and no-slip condition at the wall from Lozano-Durán & Jiménez (2014) and Lozano-Durán, Holzner & Jiménez (2016). In the following, the streamwise, wall-normal, and spanwise directions are denoted by x, y, and z, respectively. The friction Reynolds number of the simulation is $Re_\tau = u_\tau \delta / \nu \approx 950$, where u_τ is the friction velocity and δ is the channel half-height. Wall units are defined in terms of u_τ and ν and are denoted by the superscript $(\cdot)^+$. The size of the computational domain is $2\pi\delta$, 2δ, and $\pi\delta$ in the streamwise, wall-normal, and spanwise directions, respectively. The simulation is time-resolved with a time step between stored flow fields of $\Delta t^+ \approx 4$.

As before, the regularity diagnostic is applied to channel flow data by integrating only
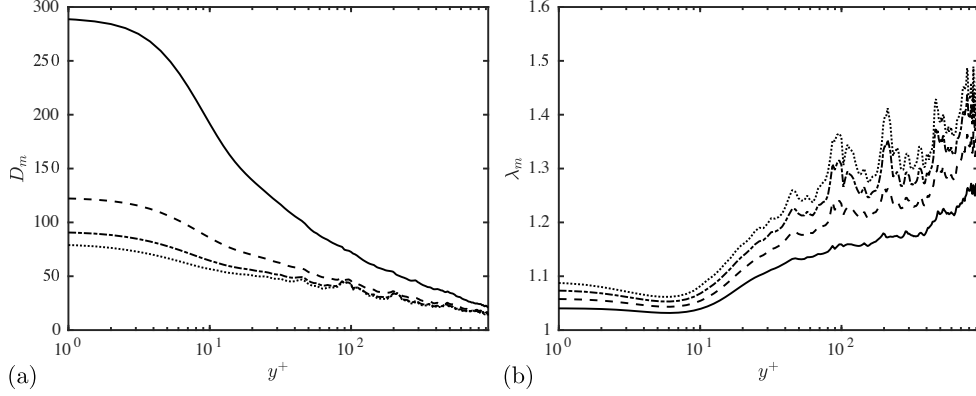
FIGURE 4. Spatial evolution of (a) D_m and (b) λ_m as a function of wall-normal height for $m = 2$ (solid), 3 (dashed), 4 (dot-dashed), 5 (dotted) for a single time instance at $Re_\tau \approx 950$.

in the homogeneous directions such that

$$\Omega_m(y,t) = \left(\frac{1}{L_x L_z} \int \int |\omega|^{2m} \mathrm{d}x\mathrm{d}z \right)^{1/(2m)}, \tag{3.1}$$

where L_x and L_z are the streamwise and spanwise computational domain lengths, respectively. D_m and λ_m are analogously defined as functions of y and t. The results for a single time instance as a function of wall-normal height are shown in Figure 4. As in the triply periodic cases, the D_m hierarchy ($D_{m+1} < D_m$) still holds for all times. The resulting λ_m spans a similar range of values as the reconnection event from Figure 4(b), and its spatial evolution is qualitatively similar to the temporal evolution of the reconnection event from Figure 3(a). The sustained value of $\lambda_m \geq 1.3$ at $y^+ \approx 100$ suggests that strong reconnection events are also present at this wall-normal height, which coincides with the wall-normal distance of the tip of hairpin vortices (Adrian 2007).

4. The (R,Q) phase plane

To further investigate regularity diagnostics on turbulent channel flows, we analyze reconnection events conditioned to the invariants of the velocity gradients tensor for incompressible flows, namely, R and Q. The approach, first introduced by Chong *et al.* (1990), has proven to be a useful tool to study flows characterized by the wide range of scales encountered in turbulence.

We consider the characteristic equation for the velocity gradient tensor for the incompressible Navier-Stokes equations given by $\lambda^3 + Q\lambda + R = 0$, where $Q = 1/2(-S_{ij}S_{ij} + R_{ij}R_{ij})$ and $R = -1/3(S_{ij}S_{jk}S_{ki} + 3R_{ij}R_{jk}S_{ki})$, with S_{ij} and R_{ij} being the strain rate and rotation rate tensors, respectively. In the present study, R and Q are computed following the grid resolution requirements provided by Lozano-Durán *et al.* (2015). The discriminant of the characteristic equation $D = 27/4R^2 + Q^3 = 0$ and $R = 0$ is used to divide the R–Q plane into four regions, as depicted in Figure 5(a). Data from different turbulent flows have shown that the joint probability density function of R and Q has a very particular skewed tear-drop shape (Martín *et al.* 1998; Ooi *et al.* 1999), with many points accumulated along the so-called Vieillefosse tail ($D = 0$ and $R > 0$).
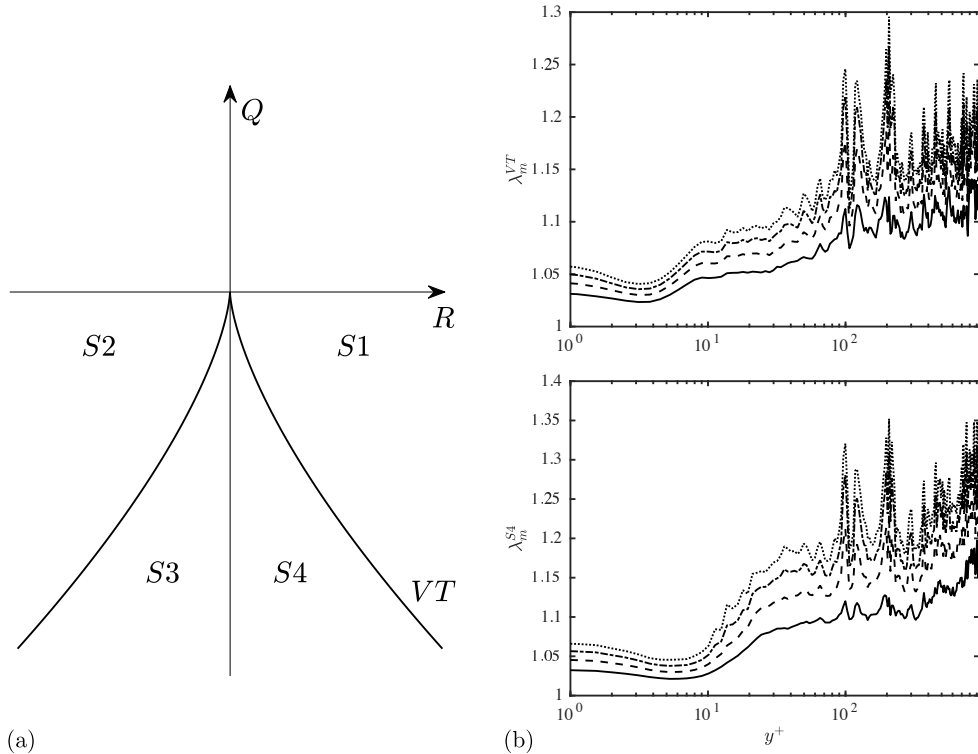
FIGURE 5. (a) Phase plane of (R, Q) invariants of the characteristic equation of the velocity gradient. Zero discriminant $D = 27/4R^2 + Q^3 = 0$ given in solid lines. Quadrants of the (R, Q) invariant plane $S1$, $S2$, $S3$, and $S4$ are labeled. VT denotes the Vieillefosse characteristic (or tail). (b) Spatial evolution of λ_m conditionally sampled on the Vieillefosse characteristic (top) and $S4$ (bottom) for the turbulent channel flow at $Re_\tau \approx 950$.

The dynamical evolution of the velocity gradient tensor has also been addressed in many statistical and reduced models. The restricted Euler equations, e.g., the time evolution of Q and R neglecting viscous and pressure effects, show that the fluid particles follow clock-wise trajectories in the R–Q plane around $R = Q = 0$ and are attracted to the Vieillefosse tail. The fourth quadrant of the (R, Q) plane ($S4$ in Figure 5a) is also notorious because it is associated with sweep and ejection events that, in turn, relate to unstable-node saddle-saddle topologies and unstable-focus compression topologies (Wallace 2016) that generate hairpin vortices (Zhou *et al.* 1999; Adrian *et al.* 2000).

Noting the aforementioned relevance of the Vieillefosse tail and $S4$ quadrant for the flow dynamics, we compute λ_m conditionally sampled to each region. The results, included in Figure 5(b), are labeled as λ_m^{S4} and λ_m^{VT} for λ_m conditionally sampled to the $S4$ quadrant and the Vieillefosse tail, respectively. Strong peaks are observed at $y^+ \approx 100$, with the largest values located in the $S4$ quadrant starting at $y^+ \approx 80$ with a maximum around $y^+ \approx 150$. This range of heights covers roughly the positions of the tips of the boundary layer hairpin vortices. The peaks decrease at larger y^+ as the hairpin vortices leave the boundary layer.
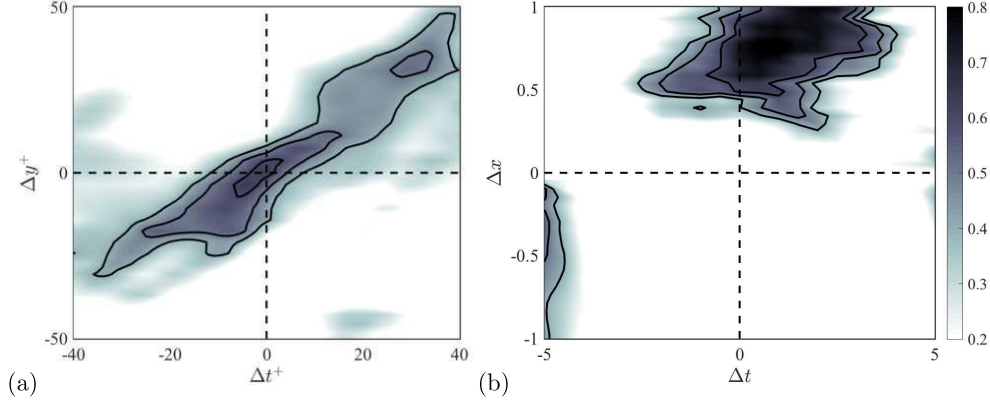
FIGURE 6. (a) Space-time correlation of $\lambda_m^{VT}(y,t)$ and $\lambda_m(y + \Delta y, t + \Delta t)$ for the turbulent channel flow at $Re_\tau \approx 950$ for $y^+ \approx 100$. (b) Space-time correlation of $\lambda_m(x_{\max}, t)$ and $\Omega_m(x_{\max} + \Delta x, t + \Delta t)$ for a vortex reconnection event with $\nu = 1.25 \times 10^{-4}$. The solid contour lines indicate correlation levels of 0.4, 0.5, and 0.6. Dashed lines are $\Delta y = 0$ and $\Delta t = 0$.

5. Space-time correlation

To demonstrate the evolution of coherent structures from the conditional regularity diagnostic on different (R, Q) quadrants, the space-time correlation of $\Omega_m(y,t)$, $D_m(y,t)$, $\lambda_m(y,t)$, and $\lambda_m(y,t)$ conditionally sampled on the four quadrants and the Vieillefosse tail are computed for the channel flow. Similarly, the space-time correlation of $\lambda_m(x,t)$, $\Omega_m(x,t)$, and $D_m(x,t)$ are studied for the reconnection event.

The space-time correlation for two vorticity moments A and B for the channel flow is defined as

$$C^{A,B}(\Delta y, \Delta t; y) = \frac{\langle A^-(y,t) \cdot B^-(y + \Delta y, t + \Delta t) \rangle_t}{(\langle A^-(y,t)^2 \rangle_t \cdot \langle B^-(y + \Delta y, t)^2 \rangle_t)^{1/2}}, \tag{5.1}$$

where the superscript $(\cdot)^-$ indicates quantities with the mean removed and $\langle \cdot \rangle_t$ indicates average in time. The results for $C^{\lambda_m^{VT}, \lambda_m}$ are given in Figure 6(a), which shows a clear diagonal shape spanning the first and third quadrant of the Δy–Δt plane. The first quadrant events correspond to the ejections and the third quadrant to the sweeps, which is consistent with the fact that $S4$ events are associated with such motions.

Similarly, the space-time correlation for vorticity moments A and B for the reconnection event is defined as

$$C^{A,B}(\Delta x, \Delta t) = \frac{\langle A^-(x_{\max}, t) \cdot B^-(x_{\max} + \Delta x, t + \Delta t) \rangle_t}{(\langle A^-(x_{\max}, t)^2 \rangle_t \cdot \langle B^-(x_{\max} + \Delta x, t)^2 \rangle_t)^{1/2}}, \tag{5.2}$$

where $x_{\max}$ is the x-location at which vorticity becomes significant ($\omega_p(x) > 0.3 \max(\omega_p)$). As demonstrated in Figure 2(b), there is a non-trivial correlation for C^{λ_m, Ω_m} in the first quadrant of the Δx–Δt plane, illustrating how λ_m precedes Ω_m both in time and space.

6. Summary

Regularity diagnostics using rescaled vorticity moments (Gibbon *et al.* 2014) are applied to high-Reynolds-number anti-parallel vortex reconnection and turbulent channel flow calculations. In both cases, we have identified events associated with values of λ_m

larger than previous computations of forced and decaying isotropic turbulence, which are indicative of stronger enstrophy growth. However, $1 \leq \lambda_m \leq 2$ (Regime I) is observed at all times. This suggests that, for both periodic domains and boundary layers, firstly, $D_{m+1} \leq D_m$ holds, where D_m is the rescaling of the Ω_m vorticity moments, and secondly, the events are regular for all times with $\lambda_m \leq 1.5$.

Application of regularity diagnostics to channel flow reveals strong peaks of λ_m at $y^+ \approx 100$. The result proves the viability of the present diagnostic for identifying intense vorticity behavior for both isolated vortex reconnection events as well as collective events characteristic of boundary layer bursts. Moreover, conditional sampling of events based on the quadrants of the (R, Q) invariant plane uncovers additional information related to the nature of the processes involved.

Future work will be devoted to conditionally sampling the space-time correlations of λ_m for different (R, Q) quadrants. The approach will help identify collective and recurring events and their associated spatio-temporal locations, as well as the details of the contributing structures. Connections with the observations reported in Kerr (2018a) regarding helicity will also be examined. To further investigate the relation between hairpin vortices and vortex reconnection events, DNS of a single time-evolving hairpin structure in wall-bounded flow will be considered (Zhou *et al.* 1999).

Acknowledgments

REFERENCES

Adrian, R. J. 2007 Hairpin vortex organization in wall turbulence. *Phys. Fluids* **19**, 041301.

Adrian, R. J., Meinhart, C. D. & Tomkins, C. D. 2000 Vortex organization in the outer region of the turbulent boundary layer. *J. Fluid Mech.* **422**, 1–54.

Ashurst, W. T., Kerstein, A. R., Kerr, R. M. & Gibson, C. H. 1987 Alignment of vorticity and scalar gradient with strain rate in simulated Navier–Stokes turbulence. *Phys. Fluids* **30**, 2343–2353.

Chong, M. S., Perry, A. E. & Cantwell, B. J. 1990 A general classification of three-dimensional flow fields. *Phys. Fluids A* **2**, 765–777.

Gibbon, J. D., Donzis, D., Gupta, A., Kerr, R. M., Pandit, R. & Vincenzi, D. 2014 Regimes of nonlinear depletion and regularity in the 3D Navier-Stokes equations. *Nonlinearity* **27**, 2605.

Kerr, R. M. 2013b Bounds for Euler from vorticity moments and line divergence. *J. Fluid Mech.* **729**, R2.

Kerr, R. M. 2013a Swirling, turbulent vortex rings formed from a chain reaction of reconnection events. *Phys. Fluids* **25**, 065101.

Kerr, R. M. 2018a Enstrophy and circulation scaling for Navier-Stokes reconnection. *J. Fluid Mech.* **839**, R2.

Kerr, R. M. 2018b Trefoil knot timescales for reconnection and helicity. *Fluid Dyn. Res.* **50**, 011422.

LOZANO-DURÁN, A. & JIMÉNEZ, J. 2014 Effect of the computational domain on direct simulations of turbulent channels up to $Re_\tau = 4200$. *Phys. Fluids* **26**, 011702.

LOZANO-DURÁN, A., HOLZNER, M. & JIMÉNEZ, J. 2015 Numerically accurate computation of the conditional trajectories of the topological invariants in turbulent flows. *J. Comput. Phys.* **295**, 805–814.

LOZANO-DURÁN, A., HOLZNER, M. & JIMÉNEZ, J. 2016 Multiscale analysis of the topological invariants in the logarithmic region of turbulent channels at a friction Reynolds number of 932. *J. Fluid Mech.* **803**, 356–394.

MARTÍN, J., OOI, A., CHONG, M. S. & SORIA, J. 1998 Dynamics of the velocity gradient tensor invariants in isotropic turbulence. *Phys. Fluids* **10**, 2336–2346.

OOI, A., MARTIN, J., SORIA, J. & CHONG, M. S. 1999 A study of the evolution and characteristics of the invariants of the velocity-gradient tensor in isotropic turbulence. *J Fluid Mech.* **381**, 141–174.

WALLACE, J. M. 2016 Quadrant analysis in turbulence research: history and evolution. *Annu. Rev. Fluid Mech.* **48**, 131–158.

ZHOU, J., ADRIAN, R. J., BALACHANDAR, S. & KENDALL, T. M. 1999 Mechanisms for generating coherent packets of hairpin vortices in channel flow. *J. Fluid Mech.* **387**, 353–396.